Optics Communications 387 (2017) 196–201

Contents lists available at ScienceDirect

Optics Communications

journal homepage: www.elsevier.com/locate/optcom

Subpixel based defocused points removal in photon-limited volumetric dataset

Inbarasan Muniraj[a], Changliang Guo[a], Ra'ed Malallah[a,b], Harsha Vardhan R. Maraka[c], James P. Ryle[a], John T. Sheridan[a,*]

[a] School of Electrical and Electronic Engineering, IOE[2] Lab, University College Dublin, Belfield, Dublin 4, Ireland
[b] Physics Department, Faculty of Science, University of Basrah, Garmat Ali, Basrah, Iraq
[c] School of Physics, University College Dublin, Belfield, Dublin 4, Ireland

A R T I C L E I N F O

Keywords:
Photon counting imaging
Three-dimensional integral imaging
Bayer Image
Image segmentation
Color image processing

A B S T R A C T

The asymptotic property of the maximum likelihood estimator (MLE) has been utilized to reconstruct three-dimensional (3D) sectional images in the photon counting imaging (PCI) regime. At first, multiple 2D intensity images, known as Elemental images (EI), are captured. Then the geometric ray-tracing method is employed to reconstruct the 3D sectional images at various depth cues. We note that a 3D sectional image consists of both focused and defocused regions, depending on the reconstructed depth position. The defocused portion is redundant and should be removed in order to facilitate image analysis e.g., 3D object tracking, recognition, classification and navigation. In this paper, we present a subpixel level three-step based technique (i.e. involving adaptive thresholding, boundary detection and entropy based segmentation) to discard the defocused sparse-samples from the reconstructed photon-limited 3D sectional images. Simulation results are presented demonstrating the feasibility and efficiency of the proposed method.

1. Introduction

The invention of three dimensional (3D) computational integral imaging (II), a technique based on Integral Photography (IP), has made auto-stereoscopic (i.e., glass free) 3D scene visualization possible [1–5]. Since its introduction, applications of II have been proposed in various research areas, e.g., 3D object sensing, biomedicine, underwater visualization, and automated target recognition [6–10]. In some special imaging cases (i.e., biomedical imaging), low-light level illumination is encountered and processing the resulting data sequences becomes necessary. Recently, one method for reconstructing multi-spectral 3D objects under photon-starved (also known as photon-limited or photon-counted) illumination conditions has been proposed [11]. It has been shown that, contrary to the conventional imaging process i.e., when dealing with three color channels independently [12], the results from multispectral imaging systems can be processed using a single channel or monochromatic system (i.e., as a greyscale image) by utilizing the Bayer patterned image sensor format [13,14]. In this way, a clear perception of the 3D scene can be achieved and it becomes much easier to interpret complex scenes and to recognize specific objects from clusters [11].

Furthermore, it has been reported that by recording high spatial frequency data, from the 3D object, high-resolution scene reconstruction is possible [15]. Capturing as many of the emanated rays as possible requires use of sophisticated cameras capable of capturing framerates of more than several hundred frames per second. This is an expensive and time-consuming process. However, in CII, a lenslet array is used to capture the diffracted rays from the 3D objects (located at some arbitrary distance from sensor). Images are recorded in the form of two dimensional (2D) the elemental images (EIs) that represent different perspectives of the captured object [6]. Back-propagation is then used to reconstruct the 3D images (also known as sectional or slice images) resulting in depth information [11]. Only the objects located at the corresponding depth distance will be simultaneously reconstructed clearly (i.e., in focus). Other points at different depths appear blurred (i.e., defocused). We note that these defocused points do not provide any useful visual information and are redundant. Therefore, they should be removed in order that better 3D visualization can take place. The resulting datasets will then aid in high-level image analysis [16].

In the field of computer vision, recovering depth information from defocused points is an important problem. To achieve this, various approaches such as stereo matching, depth from defocus (DFD), and entropy based estimation have been proposed [17–20]. Previously,

* Corresponding author.
E-mail address: john.sheridan@ucd.ie (J.T. Sheridan).

http://dx.doi.org/10.1016/j.optcom.2016.11.047
Received 16 September 2016; Received in revised form 9 November 2016; Accepted 19 November 2016
0030-4018/

such approaches have been examined to enhance 3D-II visualization [21–26]. For example, Hong et al. [21], presented a block comparison algorithm to extract the depth information from reconstructed 3D sectional images. Jang et al. [22] demonstrated a method for extracting the depth information using the correlation between a captured elemental image and a 2D periodic function. In 2004, Park et al. [23] proposed a depth location method using a correlation based multi-baseline stereo technique applied to horizontally modified elemental images, known as sub-images. In [24], Yoo applied a block matching algorithm to 3D slice image pairs (i.e., reconstructed from low-resolution EIs) to extract the depth information. Recently, Doron et al. [25] proposed an adaptive thresholding based wavelet filtering technique to extract depth from the single reconstructed photon-limited sectional image. In an extension, in [26], they also demonstrated a noise-resistant method to automatically detect the unknown depth locations of 3D objects without prior information. In addition to these, similar approaches have been examined, for use with digital in-line holographic microscopy (DIHM) techniques. For instance, image segmentation based border detection has been demonstrated to identify points in focus [27]. More recently, a method to extending the depth of field (DOF) of DIHM has also been reported [28].

Therefore, reconstructing 3D sectional image without defocused data has the effect of augmenting visualization of the 3D scene. In this paper, we present a robust subpixel accurate three-step approach (i.e., applying adaptive thresholding, boundary detection and entropy based segmentation) in order to eradicate the defocused samples from the reconstructed multispectral 3D photon-counted sectional images. The proposed method efficiently eliminates the out of focus points allowing better 3D scene visualization to be achieved. Using the method only the in-focus 3D image data is processed. Since the defocused data points are set equal to zero, the reduced datasets simplify high-level image analysis e.g. involving object tracking, classification and navigation.

The paper is organized as follows: In Section 2, we first review the 3D image capturing process. Reconstruction using maximum likelihood estimator and image interpolation are then briefly presented. The proposed segmentation technique is described in Section 3. The simulated results are presented in Section 4 and finally a brief conclusion and discussion are given in Section 5.

2. Photon-counted integral imaging (PCII)

In the case of integral imaging, if the entire scattered wave information (intensity, wavelength, and polarization) from a 3D object is recorded (this process is referred to as the Pick-up Method), an autostereoscopic 3D sectional image visualization can be achieved by applying the inverse process of the pick-up method. This inverse process is known as Scene Reconstruction. The 3D scene reconstruction can be performed using the captured data either optically [6–8] or using digital computational techniques [14].

2.1. Pick-up method

In the pick-up process, the light rays scattered from the 3D object are captured using the lenslet array. Lenslet arrays consist of periodic micro lenses that allow the capture of wide-angle light information. In the reconstruction stage, the captured light information is back-projected to reconstruct the 3D scene. Capturing wide-angle light rays increase the field of view (FOV) [5]. Fig. 1 illustrates the recording setup of a 3D object. Using such a setup, the 3D object located at an arbitrary distance (d_0) from the pick-up plane (sensor) is imaged as shown. Here, f represents the focal length of the lenslet and it is assumed $d_0 \gg f$.

Multiple 2D elemental images (EIs) are captured in an Elemental Image Array (EIA). Each EI represent a different perspective (wide-angle view) of the 3D object. In CII, by translating the Bayer formatted (described below) imaging sensor, in equal horizontal and vertical

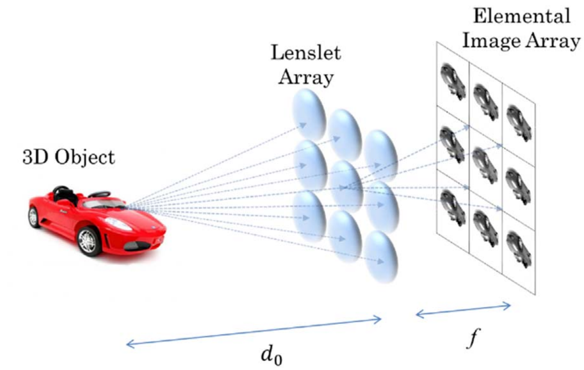

Fig. 1. Schematic setup for object sensing in II system.

(sh_x, sh_y) steps the EIA is captured. The photon-limiting method is then applied to the captured EIA. It is known that, in the photon limiting case, the Poisson distribution can be used and describes the number of times a random event occurs in a given amount of time, distance and area [29]. Thus, the uncertainty associated with the number of photons incident on a fixed sensor region for a known exposure time can be modelled using the Poisson distribution. In such a case, the probability of detecting C photons at any arbitrary pixel point (x, y) is given by C_B, and irradiance image is represented by I_B[11],

$$P(C_B; I_B) = \frac{[I_B]^{C_B}}{C_B!} e^{-I_B}, \quad g.t. \quad C_B = 0, 1, 2, 3, \ldots \tag{1}$$

where $C_B; I_B = Poisson(nI_B)$; subscript B denotes individual red, green or blue channels, n denotes the number of photons applied. It is worth mentioning that after photon-counting, the PC-EIA images can be approximated as binary data with little error [30]. After being individually processed, the photon limited monochrome channels are then superimposed to generate the photon-limited Bayer elemental images [11].

2.2. Scene reconstruction

Fig. 2 illustrates the setup of the reconstruction process modelled during Computational Integral Imaging (CII).

In this paper, we discussed one possible way to perform 3D reconstruction, Computational Integral Imaging Reconstruction (CIIR) [14]. In this approach, the 3D object data captured is reconstructed by a process known as geometric ray back propagation. This process magnifies the captured EI's, depending on the distance (d_0), to the reconstruction plane. Consequently, the magnified elemental images overlap. The objects originally located at the captured depth (d_0) appear in focus while the others are out of focus (defocused). The magnification factor $M_0 = \frac{d_0}{f}$, where f is the distance between pick up

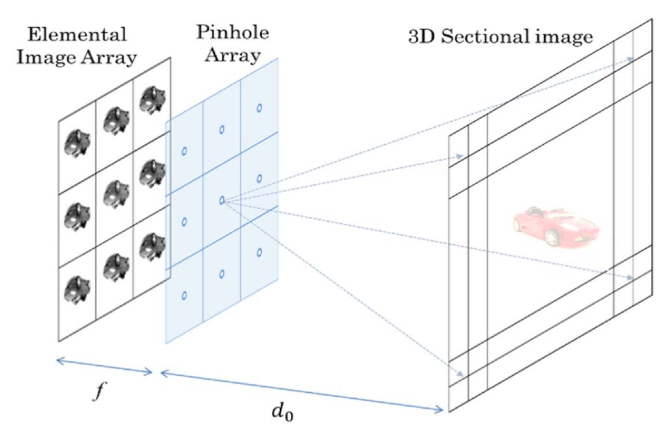

Fig. 2. 3D object reconstruction using a pinhole array in the CII system.

grid and the imaging plane as shown in Fig. 1. The object distance from the lens is denoted as d_0. The 3D reconstructed sectional image at some arbitrary distance d_0 is given as [11],

$$I(x, y, d_0)=\frac{1}{RS}\sum_{r=0}^{R-1}\sum_{s=0}^{S-1} I_{rs}\left[x+\left(\frac{sh_x}{M_0}\right)r,\ y+\left(\frac{sh_y}{M_0}\right)s\right] \tag{2}$$

where $I_{rs}[\bullet]$ represents 2D elemental image, subscripts r, s indicates the location of 2D elemental images, in the pickup grid. sh_x, sh_y denotes the shifted position of the imaging camera in horizontal (x) and vertical (y) directions. For the low-light level case, a maximum likelihood estimator (MLE) is derived to reconstruct the 3D scene [11]. It is defined as follows:

$$MLE(I_p^z)=\frac{1}{nRS}\sum_{r=1}^{R}\sum_{s=1}^{S} \boldsymbol{C}_{rs}\left(x+\left(\frac{sh_x}{M_0}\right)r,\ y+\left(\frac{sh_y}{M_0}\right)s\right), \tag{3}$$

where $\boldsymbol{C}_{rs}(\bullet)$ is the photon-counted pixel value in the rsth EI. The ML estimate of the irradiance, I_p^z, is proportional to the average of the corresponding observed samples in the elemental images. As can be seen from Eq. (2), a 3D sample point can be derived using the captured 2D elemental images. Thus, the corresponding individual values in the elemental image can be viewed as the 3D sample points [16].

2.3. Gradient based image interpolation

As mentioned above, the elemental images are captured using the Bayer color filter array (CFA). Fig. 2 shows the Bayer mosaic image pattern [31].

As can be seen from Fig. 3, the Bayer sensor captures only one of the primary color samples such as Red (R), Green (G) or Blue (B) at each pixel location (i, j). Therefore the unprocessed raw image (i.e., not interpolated) resembles 3 superimposed separate patterns or greyscale images [31]. As mentioned above, in this study, we capture Bayer formatted elemental images and then we use the gradient based interpolation (demosaicing) technique proposed by Laroche and Prescott, to convert the Bayer EIA into 3 channel multispectral data [32]. The method utilizes the fact that the human eye is more sensitive to luminance changes (i.e., the Green samples) rather than chrominance elements (i.e., Red and Blue sample values). Demosaicing is carried out as follows. In the first step, luminance channel (G) is interpolated. The second and third steps involve interpolating the gradient value, which is obtained by finding the color differences ($R-G$, $B-G$) in both the horizontal and vertical directions. Corresponding interpolated gradient values are then used to reconstruct the chrominance channels. For instance, if we need to estimate G_{43} (i.e., the missing Green value at Blue pixel B_{43} location), they are calculated as follows [32]:

$$G_{43}=\begin{cases}\frac{G_{42}+G_{44}}{2}, \text{if} \alpha<\beta\\ \frac{G_{33}+G_{53}}{2}, \text{if} \alpha>\beta\\ \frac{G_{33}+G_{42}+G_{44}+G_{53}}{4}, \text{if} \alpha=\beta,\end{cases} \tag{4}$$

where $\alpha=abs\left[\frac{(B_{41}+B_{45})}{2}-B_{43}\right]$ and $\beta=abs\left[\frac{(B_{23}+B_{63})}{2}-B_{43}\right]$, [32]. α and β are referred to the gradient values (also known as classifiers). Similarly, to find G_{34} the following classifiers are used:

$$G_{34}=\begin{cases}\frac{G_{33}+G_{35}}{2}, \text{if} \alpha<\beta\\ \frac{G_{24}+G_{44}}{2}, \text{if} \alpha>\beta\\ \frac{G_{24}+G_{33}+G_{35}+G_{44}}{4}, \text{if} \alpha=\beta,\end{cases} \tag{5}$$

In this case, $\alpha=abs\left[\frac{(R_{32}+R_{36})}{2}-R_{34}\right]$, and $\beta=abs\left[\frac{(R_{14}+R_{54})}{2}-R_{34}\right]$ [32]. Finally, the chrominance values are found from the differences between the color and luminance channels ($R-G$, $B-G$):

$$R_{33}=\begin{cases}\frac{(R_{32}-\boldsymbol{G}_{32})+(R_{34}-\boldsymbol{G}_{34})}{2}+G_{33},\\ \frac{(R_{34}-\boldsymbol{G}_{34})+(R_{54}-\boldsymbol{G}_{54})}{2}+G_{44},\\ \frac{(R_{32}-\boldsymbol{G}_{32})+(R_{34}-\boldsymbol{G}_{34})+(R_{52}-\boldsymbol{G}_{52})+(R_{54}-\boldsymbol{G}_{54})}{4}+G_{43},\end{cases} \tag{6}$$

We note that the luminance channel values must be estimated before this step (note the boldface$\boldsymbol{G}$). The same procedure can also be used to derive the Blue channels. We note that this algorithm minimizes the color artifacts without adding unnecessary complexity to the interpolation process [32].

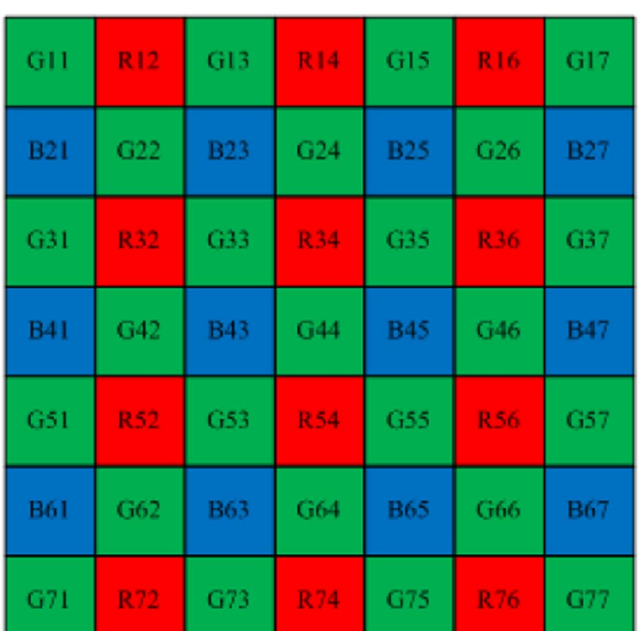

Fig. 3. Bayer mosaic (GRBG) for color image capture by a CCD sensor. $(R/G/B)_{i\ j}$ indicates the intensity of Red, Green, and Blue values at the pixel coordinate (i, j). (For interpretation of the references to color in this figure legend, the reader is referred to the web version of this article.)

3. Segmentation

In image processing, segmentation means partitioning or subdividing an image so that a detailed prescription can be achieved. It is widely applied to find or count small objects within a cluster, and for classification, recognition and tracking [33,34]. Under photons-limited conditions (<1000 photons per scene), image visualization is difficult and can lead to incorrect interpretations due to reduced image clarity. In such cases, it is hard to differentiate foreground (in focus) and background (defocused) pixels. Therefore, it is worthwhile investigating the applications of image segmentation algorithms to photon-limited integral imaging systems in order to improve 3D visualization and high-level 3D image analysis [25,26]. The process of employing segmentation algorithms is now discussed.

3.1. Subpixel division

In PCII, the normalized pixel intensities are in the range of [0, 3.4×10^{-4}]. From the Eq. (1), the probability of detecting more than one photon per pixel is relatively low (p~0.0462). However, under such conditions, i.e., involving in a computational photon-counting process, Poisson statistics can be employed and it is assumed that each pixel has more than one photon incident. For instance, in a 1000 photons per EI case, the synthesized EI will have, in total, 1000 photons. Additionally, there is a chance that a single pixel can have more than one photon in a given time interval (i.e. exposure time). Therefore, in order to precisely define the edges in the given 3D sectional PCII, we carry out subpixel level detection. When carrying out subpixel level analysis (see Fig. 4),

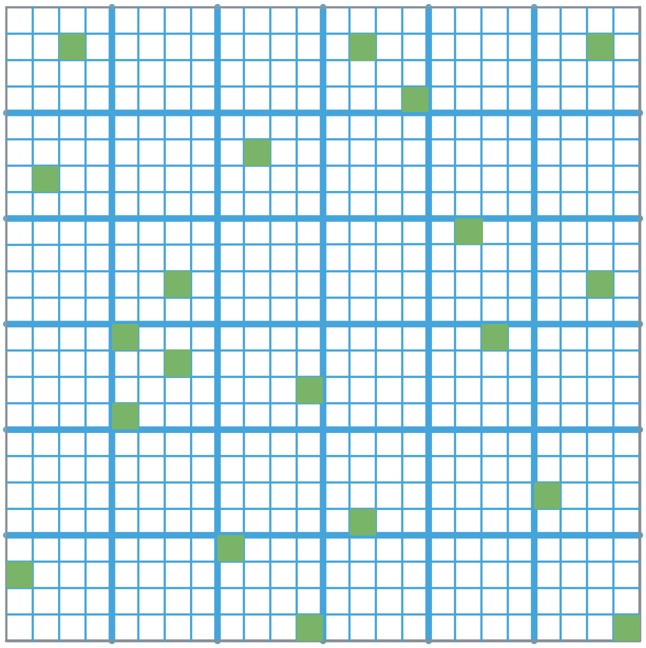

Fig. 4. Illustration of N×N (i.e., 6×6) pixel array. Each pixel is subdivided into M×M (i.e., 4×4) subpixel divisions. (For interpretation of the references to color in this figure, the reader is referred to the web version of this article.)

the reconstructed PCII images is subdivided so that photons distribution can be precisely examined. As a consequence, better performance in edge detection can be achieved.

Let us assume, the 3D photon-limited sectional image is of the size of a $N \times N$ pixel and each pixel is subdivided into $M \times M$ subpixels, where $M \ll N$ is a natural number. In Fig. 4, the thick blue lines delineate the sensor pixels while thinner blue line indicate the subpixels. Green dots identify the random locations of photon counts (a 20 photon case is given here). As can be seen, the simulated photons are scattered around the image. As noted, there is a chance that a single pixel can have more than one photon incident. If such a precise detection technique were available, it would be useful for objects tracking in video sequences [35].

3.2. Adaptive thresholding

Thresholding techniques are widely used to segment or differentiate between the foreground and background pixels in an image [27]. Simple thresholding methods will not, in general, give better results for non-uniformly illuminated scenes or irregular (noisy) background images. In such cases, a more sophisticated approach is desired. Here we employed an adaptive threshold method, based our knowledge of the mean and variance of the non-zero samples, in order to extract defocused object image data from the reconstructed image, $P_B^z(v)$. To do so we applied the thresholding function:

$$I_p^z(v) = \begin{cases} 0 & \hat{I}_{mn}^z(x, y) > \quad T \\ \bar{I}_{mn}^z & \hat{I}_{mn}^z(x, y) \leq \quad T \end{cases}, \tag{7}$$

where $\bar{I}_{mn}^z$, $\hat{I}_{mn}^z$ represent the mean (μ) and variance (σ^2) values respectively of the non-zero pixel intensities in the reconstructed 3D PC sectional image. The subscripts m, n denote the pixel locations, v represent a voxel position and z refers to the particular image depth. We note the points that are in focus on the reconstructed image will have similar mean values to the generated photon-limited elemental images. In addition, the variance of the focused 3D points would be small compared to the variance of the defocused 3D points. Therefore, a threshold value can be used to find whether a pixel value should be retained or eliminated.

$$\begin{bmatrix} +1 & 0 \\ 0 & -1 \end{bmatrix} \qquad \begin{bmatrix} 0 & +1 \\ -1 & 0 \end{bmatrix}$$

(a) (b)

Fig. 5. Roberts Cross convolution kernels: (a) Kernel G_x, (b) Kernel G_y.

3.3. Boundary detection (BD)

In general, digital images can be thought of as consisting of various boundaries (i.e., edges) created by changes in cues such as color, texture, or phase. Usually, such edges are detected by measuring discontinuities in brightness in the image. Edge descriptor is high spatial frequency content dominates the visual information. Such information is important when implementing edge or boundary detection (BD) algorithms in image segmentation applications. Ideally, a BD algorithm will identify and trace out the exterior boundaries as well as the boundaries of any 'holes' present in the image [27]. In general, any gradient operators will work well in detecting the boundaries of isolated objects. Therefore, we employed the Robert cross operators (see Fig. 5) in order to detect the edges in focus data location in the reconstructed 3D image [36]. In the resulting output images each pixel value represent the estimated absolute magnitude of the spatial gradient of the corresponding input pixel:

$$|G| = \sqrt{G_x^2 + G_y^2} \tag{8}$$

where G_x,G_y denotes the first and second kernels. Theoretically, this operator consists a pair of 2×2 convolution kernels. Fig. 5 shows the two convolution kernels used.

It is to be noted that G_y is G_x rotated by 90° anticlockwise.

3.4. Entropy criterion

In addition to the above, we also have considered the use of image entropy values to identify in focus image data. Theoretically, entropy is a statistical measurement of the disorder within an image that can be used to characterize the texture of the object. It is derived as follows [28].

$$Entropy = \quad -\sum (h.^{*}\log_2(h)) \tag{9}$$

where h denotes the sub-image histogram counts. A sharp edged or focused object in a given 3D sectional image possesses lower entropy than one that is defocused.

4. Simulation results

In order to test our approach the proposed adaptive segmentation technique was applied to reconstructed photon-limited 3D sectional images. The resulting simulations are presented in this section. Assuming color imaging, we processed PCI for three color channels. At first, the color channels (R, G, and B) are segregated independently and the empty pixels are set to zero. After individually performing photon-counting the separated color channels are merged to generate the original Bayer format. Finally, the photon counted Bayer elemental images are used in reconstruction, see Section 2.3. A standard demosaicing algorithm is applied to the Bayer patterned 3D sectional images to convert them into a single multispectral 3D scene. We note that processing the Bayer image is computationally more feasible than dealing directly with the corresponding RGB image [11].

A 3D scene, see Fig. 6(a), consisting of a tricolored ball (Object 1) and an angry bird toy (Object 2) is considered in our simulations. Both objects were positioned at different locations, displaced from the

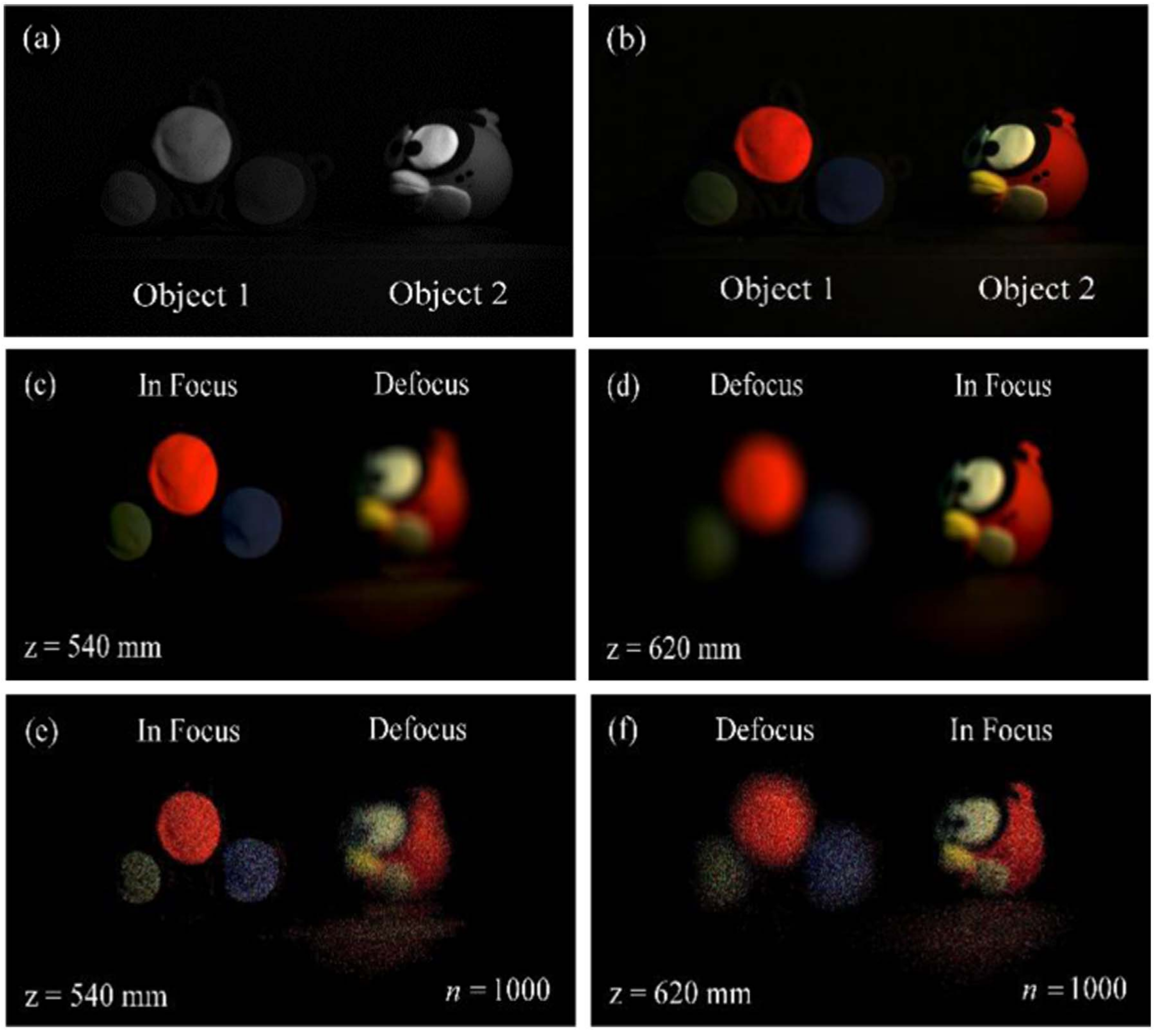

Fig. 6. Integral Images: (a) Raw Bayer pattern center EI; (b) interpolated multispectral version of (a); (c) reconstructed 3D sectional image when Object 1 is in focus (z=540 mm); (d) reconstructed 3D sectional image when Object 2 is in focus (z=620 mm); (e) photon-counted version of (c); (f) photon-counted version of (d). (For interpretation of the references to color in this figure, the reader is referred to the web version of this article.)

imaging sensor, which is in the imaging plane. The captured data consisted of $10 Columns \times 10 Rows$ Bayer patterned 2D EIs each with an image size of 1024×1024 pixels and having 8 bits per pixel. Fig. 6(a) shows the captured 2D EI (at center location) in Bayer format. Fig. 6(b) shows the interpolated version of Fig. 6(a) using the method described in Section 2.3. Fig. 6(c) and (d) show the reconstructed (generated using the ray back-propagation method described in Section 2.2), 3D sectional images. Examining Fig. 6(c), at one particular depth (z=540 mm), it can be seen that Object 1 is clearly focused (i.e., well defined edges) while Object 2 is defocused. Similarly, in Fig. 6(d) Object 2 is in focus at depth z=620 mm while Object 1 is out of focus. In Fig. 6(e) and (f) the corresponding photon-limited (n = 1000) 3D sectional images, reconstructed using MLE method as described in Eq. (3).

As noted, examining, Fig. 6(c)–(f), we can conclude that only at one depth location is one of the 3D objects clearly in focus while the other is defocused. Therefore, we can now apply the adaptive segmentation method described in Section 3, to discard the defocused objects from the sectional images. Fig. 7 shows the resulting 'cleaned up' depth images.

Finally, we calculated the entropy values of both the objects in Fig. 6(e) and (f), respectively. Examining the resulting values in Table 1, it is clear that the focused data (i.e., defined edges and slowly varying background) has lower entropy compared to a defocused data (resembles noisy image whose pixel values scattered) without a well-defined or ordered structure.

Furthermore, such entropy values can be used extract the defocused data and then only the surface corresponding to the focused volume data is retained [37].

5. Conclusion

In this study, we presented a method for simultaneous reconstruction of multiple 3D sectional images, while eliminating out of focused points, in a photon-counted multispectral computational integral imaging system (PCII). At first, 2D Bayer formatted elemental images are captured and processed. Poisson statistics are applied to the segregated individual color channels. Then, the resulting photon limited EIA is utilized for 3D scene reconstruction using maximum likelihood estimation (MLE). Finally, the Bayer patterned 3D sectional images (resembling greyscale images) are interpolated to perform multispectral visualization using the gradient based image interpolation technique. As noted, photon-limited images show a greater potential for compression with higher compression ratio (i.e., 3D frames can be transmitted using lower bitrates).

As shown reconstructed 3D sectional images consist of both focused and defocused data points that correspond to the relative depth positions. The defocused points present degrade the image quality and act as a barrier to efficient high-level image analysis. To overcome this limitation, subpixel level based three-step technique (i.e., employ-

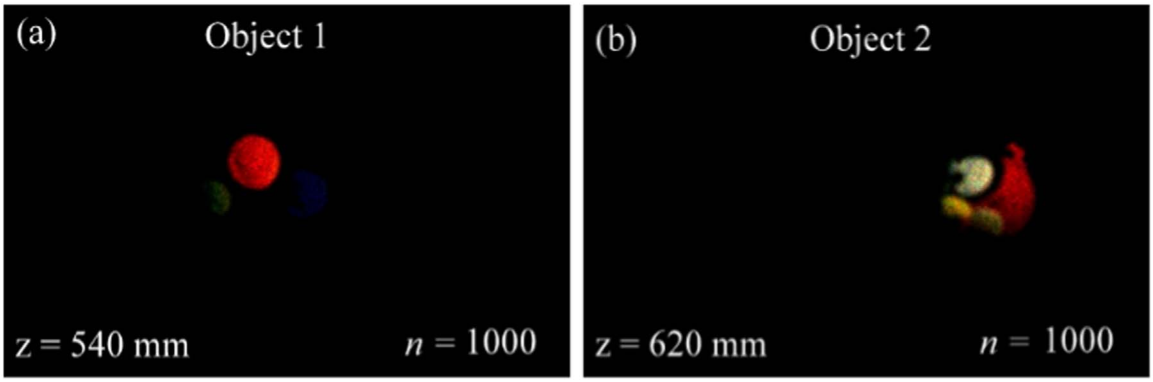

Fig. 7. In focused only segmented 3D sectional images (1000 photons per scene): (a) Reconstructed image at depth (z=540 mm), (b) reconstructed 3D scene at depth (z=620 mm).

Table 1
Entropy values of reconstructed 3D sectional images at different depths.

Entropy values		
Distance	z_1=540 mm	z_2=620 mm
3D Object 1	1.04 (in focus)	1.35 (defocus)
3D Object 2	1.44 (defocus)	1.05 (in focus)

ing adaptive thresholding, boundary detection and entropy based segmentation) is used to discard the defocused samples from the reconstructed photon-limited 3D sectional images. Based on our analysis, we conclude that the adjacent pixel intensities are highly correlated in an image. Taking this fact into account uncorrelated background pixel can be easily identified and discarded.

This work should assist high-level image analysis. It is intended to extend our approach to tackle more complex scenarios such as tracking and segmenting of images captured using digital hologram based microscopic systems.

Funding sources and acknowledgments

IM acknowledges the support of Irish Research Council (IRC). CG is supported under the UCD-China Scholarship Council (UCD-CSC) program. R. Malallah is supported by the Iraqi Ministry of Higher Education and Scientific Research. HVRM, JPR, JTS thanks Science Foundation Ireland (SFI), and Enterprise Ireland (EI) under the National Development Plan (NDP).

References

[1] M.G. Lippmann, Epreuves reversible donnant la sensation du relief, J. Phys. 7 (1908) 821–825.
[2] H.E. Ives, Optical properties of a Lippmann lenticulated sheet, J. Opt. Soc. Am. 21 (1931) 171–176.
[3] T. Okoshi, Three Dimensional Imaging Techniques, Academic, New York, 1971.
[4] F. Okano, H. Hoshino, J. Arai, I. Yuyama, Real-time pickup method for a three-dimensional image based on integral photography, Appl. Opt. 36 (1997) 1598–1603.
[5] M.M. Corral, B. Javidi, R.M. Cuenca, G. Saavedra, Integral imaging with improved depth of field by use of amplitude-modulated microlens arrays, Appl. Opt. 43 (2004) 5806–5813.
[6] B. Javidi, F. Okano (Eds.), Three Dimensional Television, Video, and Display Technologies, Springer, Berlin, 2002.
[7] A. Stern, B. Javidi, Three-dimensional image sensing, visualization, and processing using integral imaging,, IEEE 94 (2006) 591–607.
[8] J.H. Park, K. Hong, B. Lee, Recent progress in three-dimensional information processing based on integral imaging, Appl. Opt. 48 (2009) H77–H94.
[9] M. Cho, M. Daneshpanah, I. Moon, B. Javidi, Three-dimensional optical sensing and visualization using integral imaging, IEEE 99 (2011) 556–575.
[10] H. Liao, N. Hata, S. Nakajima, M. Iwahara, I. Sakuma, T. Dohi, Surgical navigation by autostereoscopic image overlay of integral videography, IEEE Trans. Inf. Technol. Biomed. 8 (2004) 114–121.
[11] I. Moon, I. Muniraj, B. Javidi, 3D visualization at low light levels using multi-spectral photon counting integral imaging, J. Disp. Technol. 9 (2013) 51–55.
[12] B. Chen, H. Shu, G. Coatrieux, G. Chen, X. Sun, J.L. Coatrieux, Color image analysis by quaternion-type moments, J. Math. Imaging Vis. 51 (2015) 124–144.
[13] I. Muniraj, C. Guo, B.G. Lee, J.T. Sheridan, Interferometry based multispectral photon-limited 2D and 3D integral image encryption employing the Hartley transform, Opt. Express 23 (2015) 15907–15920.
[14] I. Muniraj, S. Rajasekaran, C. Guo, J.T. Sheridan, Multispectral single-channel 3D computational integral imaging using compressive sensing, FTh1F.3, Frontiers in Optics, 2015.
[15] Y. Choi, T.D. Yang, C.F. Yen, P. Kang, K.J. Lee, R.R. Dasari, M.S. Feld, W. Choi, Overcoming the diffraction limit using multiple light scattering in a highly disordered Medium, Phys. Rev. Lett. 107 (2011) 023902–023904.
[16] F. Yi, J. Lee, I. Moon, Simultaneous reconstruction of multiple depth images without off-focus points in integral imaging using a graphics processing unit, Appl. Opt. 53 (2014) 2777–2786.
[17] A.P. Pentland, A new sense for depth of field, IEEE Trans. Pattern Anal. Mach. Intell. 9 (1987) 523–531.
[18] V.M. Bove, Entropy-based depth from focus, J. Opt. Soc. Am. A 10 (1993) 561–566.
[19] J. Ens, P. Lawrence, An investigation of methods for determining depth from focus, IEEE Trans. Pattern Anal. Mach. Intell. (1993) 97–107.
[20] A.N. Rajagopalan, S. Chaudhuri, A variational approach to recovering depth from defocused images, IEEE Trans. Pattern Anal. Mach. Intell. 19 (1997) 1158–1164.
[21] S.P. Hong, D. Shin, B.G. Lee, E.S. Kim, Depth extraction of 3D objects using axially distributed image sensing, Opt. Express 20 (2012) 23044–23052.
[22] J.Y. Jang, J.I. Ser, S. Cha, S.H. Shin, Depth extraction by using the correlation of the periodic function with elemental image in integral imaging, Appl. Opt. 51 (2012) 3279–3286.
[23] J.H. Park, S. Jung, H. Choi, Y. Kim, B. Lee, Depth extraction by use of rectangular lens array and one-dimensional elemental image modification, Appl. Opt. 23 (2004) 4882–4895.
[24] H. Yoo, Depth extraction for 3D objects via windowing technique in computational integral imaging with a lenslet array, Opt. Lasers Eng. 51 (2013) 912–915.
[25] D. Aloni, Y. Yitzhaky, Detection of object existence from a single reconstructed plane obtained by integral imaging, IEEE Photonics Technol. Lett. 26 (2014) 726–728.
[26] D. Aloni, Y. Yitzhaky, Automatic 3D object localization and isolation using computational integral imaging, Appl. Opt. 54 (2015) 6717–6724.
[27] K.M. Molony, J.P. Ryle, S. McDonnell, J.T. Sheridan, T.J. Naughton, Segmentation and visualization of digital in-line holographic microscopy of three-dimensional scenes using reconstructed intensity images, Proc. SPIE 7443 (2009) 74431F.
[28] J.P. Ryle, S. McDonnell, B. Glennon, J.T. Sheridan, Calibration of a digital in-line holographic microscopy system: depth of focus and bioprocess analysis, Appl. Opt. 52 (2013) C78–C87.
[29] J.W. Goodman, Statistical Optics, Wiley Classics Library Etd, 2000, pp. 85–99.
[30] B. Tavakoli, B. Javidi, E. Watson, Three dimensional visualization by photon counting computational Integral Imaging, Opt. Express 16 (2008) 4426–4436.
[31] B.E.Bayer, Color imaging array, U.S. Patent No. 3, to Eastman Kodak Company, Rochester, NY, 1976.
[32] C.A.Laroche, M.A.Prescott, Apparatus and method for adaptively interpolating a full color image utilizing chrominance gradients, U.S. Patent. 5, to Eastman Kodak Company Rochester, NY, 1994.
[33] Y. Zheng, B. Jeon, D. Xu, Q.M.J. Wu, H. Zhang, Image segmentation by generalized hierarchical fuzzy C-means algorithm, J. Intell. Fuzzy Syst. 28 (2015) 961–973.
[34] D. Shin, B. Javidi, Three-dimensional integral imaging with improved visualization using subpixel optical ray sensing, Opt. Lett. 37 (2012) 2130–2132.
[35] D. Mas, B. Ferrer, J.T. Sheridan, J. Espinosa, Resolution limits to object tracking with subpixel accuracy, Opt. Lett. 37 (2012) 4877–4879.
[36] L.G. Roberts, Machine perception of 3-D solids, in: J.T. Tippet (Ed.)Optical and Electro-optical Information Processing, MIT Press, 1965, pp. 159–197.
[37] I.Muniraj, C.Guo, J.P.Ryle, J.T.Sheridan, Space-variant defocused content removal in Photon-counted volumetric datasets, in: Imaging and Applied Optics, JW4A.1, 2016.